Journal of Alloys and Compounds 629 (2015) 178–183

Contents lists available at ScienceDirect

Journal of Alloys and Compounds

journal homepage: www.elsevier.com/locate/jalcom

Critical behaviour of magnetic transitions in $KCoF_3$ and $KNiF_3$ perovskites

A. Oleaga [a,*], A. Salazar [a], D. Skrzypek [b]

[a] Departamento de Física Aplicada I, Escuela Técnica Superior de Ingeniería, Universidad del País Vasco UPV/EHU, Alameda Urquijo s/n, 48013 Bilbao, Spain
[b] Institute of Physics, University of Silesia, Uniwersytecka 4, Katowice 40-007, Poland

ARTICLE INFO

Article history:
Received 5 September 2014
Received in revised form 16 December 2014
Accepted 28 December 2014
Available online 8 January 2015

Keywords:
Critical behaviour
Calorimetry
Photopyroelectric
Thermal diffusivity

ABSTRACT

KAF_3 (A = Mn, Co, Ni) are considered as perfect 3-D Heisenberg antiferromagnets though there are scarce experimental evidences of that behaviour in the case of the last two perovskites. In this work, a high resolution photopyroelectric technique has been used to study the critical behaviour of the antiferromagnetic transition in $KCoF_3$ and $KNiF_3$ measuring specific heat, thermal diffusivity and thermal conductivity. The critical behaviour of $KNiF_3$ slightly deviates from the perfect Heisenberg universality class (the retrieved parameters are $\alpha = -0.110$, $A^+/A^- = 1.30$), due to its small uniaxial anisotropy; this behaviour has been confirmed by the critical parameters of both the specific heat and the thermal diffusivity. In opposition to what is assumed in literature, the critical behaviour of $KCoF_3$ cannot be simply described by the Heisenberg universality class ($\alpha = -0.081$, $A^+/A^- = 1.19$) due to the spin–orbit interaction at the magnetic transition, which introduces a perturbation in the Hamiltonian and makes the pure Heisenberg model incomplete for this case. The results for both materials disagree with and correct previous works on them.

1. Introduction

Perovskites have attracted great attention in the last decades because of several interesting properties such as high-temperature superconductivity, colossal magneto resistance and competing physical mechanisms at the magnetic transitions. Halogen based cubic perovskites ABX_3 (A and B are mono- and divalent cations and X is a monovalent halogen anion) have been extensively studied due to the variety of their electrical, optical and magnetic properties [1]. Regarding the characteristics of continuous phase transitions, the experimental study of their critical behaviour has been widely used to ascertain the validity of the universality classes, which allows to describe the underlying physical mechanisms in different kind of materials with a common model, thus getting a quick insight on the physics of the transition. In the particular case of magnetic transitions, the dimensionality of the system d and the (an)isotropy of the magnetic ordering (expressed by the number of components of the order parameter n) are the identifiers which assign the material to the Ising, XY or Heisenberg class (just to mention the most common ones) [2]. There is a wide variety of experimental variables which can be used to extract the critical behaviour (magnetic, thermal, nuclear, optical...) but some techniques are more sensitive than others in order to retrieve the critical parameters and discriminate among the models, especially if the values of those parameters are very different from one model to the next one. Besides, the high resolution techniques which allow to get closer to the critical temperature are the best ones to evaluate possible crossovers or deviations from a certain model, either because of a small anisotropy with respect to the isotropic model, or due to the presence of a perturbing second physical mechanism at the transition which introduces an additional order parameter or interactions between the two of them. In particular, thermal measurements which study the critical behaviour of the specific heat and related thermal variables (thermal diffusivity, thermal conductivity) are better suited than other techniques as the value of their critical parameters are very different in each model (see Table 1); high resolution ac photopyroelectric calorimetry has revealed as a very sensitive technique to measure thermal variables and retrieve the critical parameters with great accuracy [3–7].

Focusing our attention on fluoride perovskites, critical behaviour studies of $RbMnF_3$ and $KMnF_3$ have soundly established that they belong to the 3D-Heisenberg class, as the isotropic arrangement of their spins is nearly perfect [3,4,8,9], while the easy-plane antiferromagnet $CsMnF_3$ is a perfect 3D-XY [5] and the strongly anisotropic FeF_2 is a nice example of a 3D-Ising one [8]. $KNiF_3$

* Corresponding author. Tel.: +34 946014008.
E-mail address: alberto.oleaga@ehu.es (A. Oleaga).

http://dx.doi.org/10.1016/j.jallcom.2014.12.237
0925-8388/

and $KCoF_3$ are also generally included among the cubic perovskites, though there is a deviation from the cubic structure at the magnetic transition, small in the case of $KNiF_3$ but tetragonal in the case of $KCoF_3$. Both of them are thought to belong to the perfect 3D-Heisenberg class [10–12] but only one work has been done to evaluate this attribution, by means of linear birefringence [13].

It is worth taking into account the similarities and differences in magnetic properties among $RbMnF_3$, $KMnF_3$, $KNiF_3$ and $KCoF_3$. All of them have a G-type antiferromagnetic structure but the direction of the spins differs: in $RbMnF_3$ this is along the threefold axes, in $KMnF_3$ they are canted 43.4° with respect to the *c*-axis, in $KNiF_3$ it is along the fourfold axes and in $KCoF_3$ it is along the *c*-axis [14,15]. Another important difference is that Mn^{2+} ions have no orbital moment, while Ni^{2+} and Co^{2+} ions have, so the influence of spin–orbit interaction could and does make a difference at the transition, being more important for $KCoF_3$ than for $KNiF_3$. Lastly, uniaxial anisotropy (the ratio between the anisotropy field H_A and the exchange field H_E) has been evaluated for $RbMnF_3$ (6×10^{-6}) [16], $KMnF_3$ (5.9×10^{-6}) [17] and $KNiF_3$ (2.4×10^{-5}) [10], values which suggest that $KNiF_3$ might present differences with respect to the other two. That kind of information is not available for the case of $KCoF_3$.

Hence, the aim of this work is to perform high resolution thermal measurements to evaluate how the particularities of $KNiF_3$ and $KCoF_3$ affect the critical parameters and identify if they really belong to the 3D-Heisenberg universality class or not.

2. Samples and experimental techniques

Single crystals of $KCoF_3$ and $KNiF_3$ were grown from the melt by the horizontal Bridgman method as described in detail by Skrzypek et al. [18]. The starting stoichiometric mixtures KHF_2, CoF_2, NiF_2 were heated to maximum temperatures higher than their respective melting points by about 50 K. The single crystals were then obtained by cooling the liquid mixtures. The low cooling rates were maintained by driving the melt through the temperature gradient of the furnace at a rate of 4 mm/h. The crystallization process was performed under an argon atmosphere. The crystal structure was verified by X-ray diffraction technique. These compounds crystallized in the perovskite cubic symmetry (Pm3m). The unit-cell parameters are: 4.011(2) Å and 4.069(4) Å for $KNiF_3$ and $KCoF_3$, respectively [19]. The measurements were carried out on powdered samples from line profile measurements in similar conditions as reported in [20]. The $KNiF_3$ does not show any evidence of structural phase transitions and $KCoF_3$ undergoes a tetragonal distortion with $c/a < 1$ at 114 K according with Okazaki et al. [21]. The X-ray microanalysis technique allowed us to carry out the homogeneity analysis. The measurements were made for a few micro areas of the crystal surface (the dimensions of which were about a few hundred micrometers). The results obtained confirm the high homogeneity of the crystal examined. Slices of thickness of about 0.73 mm were used for the present study. The samples were prepared so that they had well polished, plane-parallel surfaces.

A high-resolution ac photopyroelectric calorimetry in the back detection configuration has been used in this work to extract thermal diffusivity *D*, specific heat c_p and thermal conductivity *K*. The first one is extracted from the phase of the photopyroelectric signal while a combination of amplitude and phase must be used for the other two thermal parameters. The details of the experimental setup, as well as of the theory which explains how the thermal parameters are obtained from the photopyroelectric signal can be found elsewhere [5,22–25]. The range of cooling and heating rates used has been from 60 mK/min for measurements on a wide temperature range down to 10 mK/min for high-resolution runs close to the Néel temperatures.

Table 1
Most common magnetic universality classes for $d = 3$ and the corresponding critical parameters. α and A^+/A^- are for specific heat, β for spontaneous magnetization, γ for isothermal susceptibility, ν for the correlation length.

Universality class	*n*	α	β	γ	ν	A^+/A^-
Ising	1	0.11	0.33	1.24	0.63	0.52
XY	2	−0.014	0.34	1.30	0.66	1.06
Heisenberg	3	−0.115	0.36	1.39	0.71	1.52

3. Fitting procedure

The experimental specific heat curves have been fitted to the equation:

$$c_p = B + Ct + A^{\pm}|t|^{-\alpha}(1 + E^{\pm}|t|^{0.5}), \tag{1}$$

where $t = (T - T_N)/T_N$ is the reduced temperature, T_N the critical temperature, and α, $A^{\pm}$, B, C and $E^{\pm}$ are adjustable parameters. Superscripts + and − stand for $T > T_N$ and $T < T_N$ respectively. The linear term represents the background contribution to the specific heat (which includes both the lattice and the magnetic contributions), while the last term is the anomalous contribution to the specific heat. The factor under parenthesis is the correction to scaling that represents a singular contribution to the leading power as known from experiments and theory [26,27].

A non-linear least square routine using a Levenberg–Marquardt method has been used to simultaneously fit the experimental data for $T > T_N$ and $T < T_N$. First of all, we selected a fitting range close to the transition while avoiding the rounding part, and kept fixed the value of T_N. We performed a first fitting without the correction to scaling term and obtained a set of adjusted parameters. Afterwards, we tried to increase the number of data points included in the fitting, first fixing t_{min} and increasing t_{max} up to values where no changes were detected in the fit quality, and then fixing t_{max} and decreasing t_{min} to get as close as possible to the Néel temperature, always avoiding the rounded part. The next step was to introduce the correction to scaling term in order to improve the fitting. As a last checking, we let T_N be a free parameter in order to confirm the fitting. In the whole process, we focused our attention on the root mean square value as well as on the deviation plot, which is the difference between the fitted values and the measured ones as a function of the reduced temperature. This procedure is the one commonly used for this kind of fittings [5–7,26].

Thermal diffusivity has also been used to extract information about the critical behaviour of the magnetic transition. A similar equation to Eq. (1), used for specific heat, with its own critical parameters, is written as

$$D = V + Wt + U^{\pm}|t|^{-b}(1 + F^{\pm}|t|^{0.5}) \tag{2}$$

and an equivalent procedure to the one explained above with c_p has been followed to fit the experimental results of thermal diffusivity to Eq. (2).

In order to compare the fitted parameters obtained by means of (1) and (2), we use the constitutive equation $D = \frac{K}{\rho c_p}$, where *K* stands for thermal conductivity and ρ for density, and thus write (leaving aside the correction to scaling factors, which are phenomenologically introduced only to extend the fitting range):

$$D = V + Wt + U^{\pm}|t|^{-b} = \frac{K}{\rho c_p} = \frac{K}{\rho B}\left(1 + \frac{C}{B}t + \frac{A^{\pm}}{B}|t|^{-\alpha}\right)^{-1} \tag{3}$$

Approximate relations between the parameters can be found in the Heisenberg, XY and Ising universality classes [3–6]. In particular, in the Heisenberg case, where $|t|^{-\alpha} \ll 1$, the right hand part can be developed in a Taylor series, giving

$$D = V + Wt + U^{\pm}|t|^{-b} \approx \frac{K}{\rho B}\left(1 - \frac{C}{B}t - \frac{A^{\pm}}{B}|t|^{-\alpha}\right) \tag{4}$$

From Eq. (4) we can extract the following relations among the critical parameters of the specific heat and thermal diffusivity

$$b \approx \alpha, \tag{5a}$$

$$U^{\pm} \approx -KA^{\pm}/\rho B^2 > 0 \tag{5b}$$

$$U^{+}/U- \approx A^{+}/A^{-} \tag{5c}$$

Besides, the rest of the parameters are related through

$$V \approx K/\rho B \tag{5d}$$

$$W \approx -KC/\rho B^2 \tag{5e}$$

4. Results and discussion

The thermal diffusivity as a function of temperature in a long temperature range centred at the magnetic transition for both samples is presented in Fig. 1. The general evolution is quite typical, with higher values at low temperature due to the wider length of the phonons mean free path, quickly diminishing as temperature increases, reaching at room temperature the values of 1.21 mm^2/s ($KCoF_3$) and 2.15 mm^2/s ($KNiF_3$). The inset in Fig. 1 shows the evolution of thermal diffusivity for $KCoF_3$ near room temperature in order to better compare it with $KNiF_3$. In both cases, the antiferromagnetic transition is manifested as a dip superimposed on the thermal diffusivity curve. The Néel temperatures are, respectively, 115.3 K and 244.8 K, in agreement with literature [28–30]. It is worth pointing out that no thermal hysteresis appears in any of the thermal variables in any sample, within our experimental uncertainty. Besides, the shapes are consistent with continuous transitions.

Figs. 2 and 3 show the high resolution curves for thermal diffusivity, specific heat and thermal conductivity in the case of $KNiF_3$ and $KCoF_3$, respectively, in the near vicinity of the Néel temperature as a function of the reduced temperature $t = (T - T_N)/T_N$. Specific heat and thermal conductivity are always noisier than thermal diffusivity using this technique, as the latter is obtained only using the phase of the photopyroelectric signal while for the former two both amplitude and phase are needed. Specific heat shows the usual lambda-shape associated to second-order phase transitions; concerning thermal conductivity, there is only a change of slope at the transition, which is bigger in the case of $KNiF_3$ than in the case of $KCoF_3$ (see Figs. 2e and 3e).

Starting with $KNiF_3$, the fitted curve for specific heat is superimposed to the experimental data points in Fig. 2a, in which the dots correspond to the experimental data (not all of them have been presented, for the sake of clarity) and the continuous lines to the best fitting to Eq. (1). As can be seen in Fig. 2a, the fitting is very good. In order to better evaluate the quality of the fittings, Fig. 2b shows the deviation plots of the fitting with respect to the experimental curve. Again, not all points are presented, for the sake of clarity.

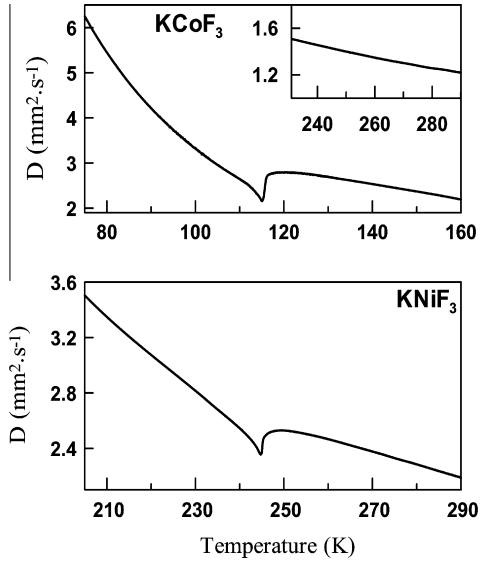

Fig. 1. Thermal diffusivity as a function of temperature for $KCoF_3$ and $KNiF_3$. The inset shows the behaviour near room temperature for $KCoF_3$.

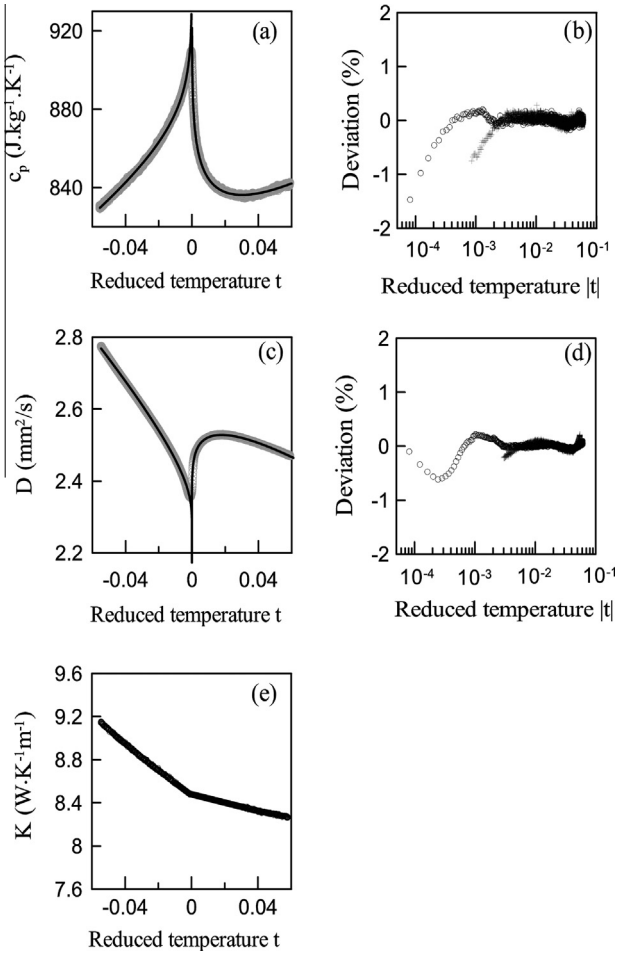

Fig. 2. Experimental (dots) and fitted curves (continuous lines) of the specific heat (a), thermal diffusivity (c) and thermal conductivity (e) as a function of the reduced temperature for the antiferromagnetic to paramagnetic transition in $KNiF_3$. (b) and (d) present the corresponding deviation plots. Open circles are for $T < T_N$ and crosses for $T > T_N$. Not all experimental points are shown, for the sake of clarity.

The fitting ranges are in all cases limited by the rounding in the curves; this rounding is inherent to the samples and not attributable to the technique, as shown elsewhere [7].

The values of the critical parameters, the fitting ranges and the quality of the fittings given by the root mean square value are presented in Table 2. The values of the critical exponent $\alpha = -0.110 \pm 0.003$ and the ratio of the coefficients $A^+/A^- = 1.30 \pm 0.03$ agree quite well with the theoretical values for the 3D-Heisenberg universality class though there is a small deviation in the ratio, reducing its value (which is 0.52 for the uniaxial Ising class). This is surely due to the fact that there is a small uniaxial magnetic anisotropy [10] with a slightly distorted cubic structure, which makes $KNiF_3$ not as perfect a Heisenberg antiferromagnet as KMnF3 or $RbMnF_3$, where the critical exponents of both specific heat and thermal diffusivity comply with that universality class, fulfilling Eq. (5) [3,4]. Uniaxial anisotropy (the ratio between the anisotropy field H_A and the exchange field H_E) is 2.4×10^{-5} in $KNiF_3$ [10] while it is 5.9×10^{-6} in $KMnF_3$ [17] and 6×10^{-6} in $RbMnF_3$ [16]. Even if the values are small, the difference is of an order of magnitude, which could simply imply small deviations in the critical parameters from the theoretical values of the Heisenberg universality class, as it happens. It is well known from renormalization group theory that the presence of a small

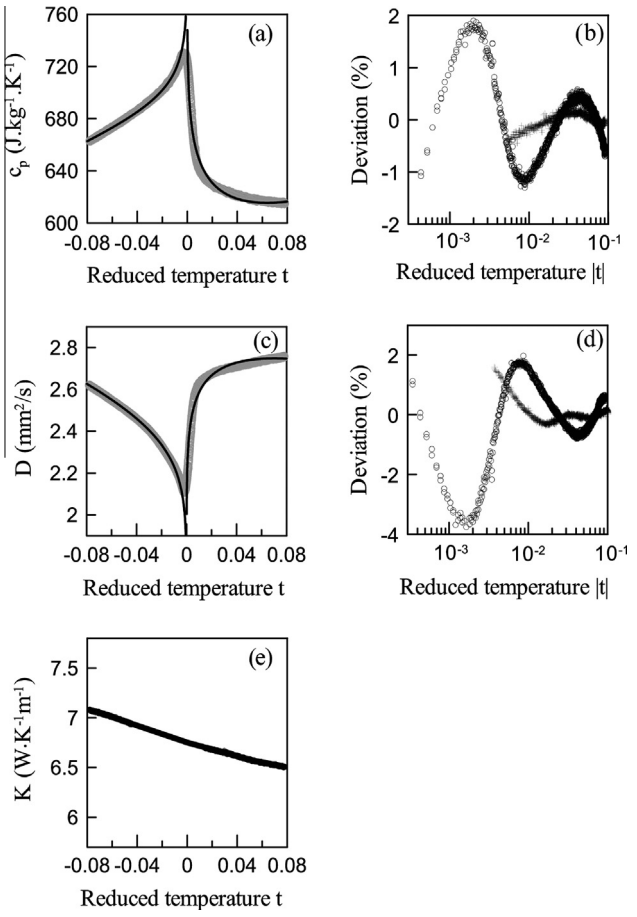

Fig. 3. Experimental (dots) and fitted curves (continuous lines) of the specific heat (a), thermal diffusivity (c) and thermal conductivity (e) as a function of the reduced temperature for the antiferromagnetic to paramagnetic transition in $KCoF_3$. (b) and (d) present the corresponding deviation plots. Open circles are for $T < T_N$ and crosses for $T > T_N$. Not all experimental points are shown, for the sake of clarity.

anisotropy can produce a crossover from the 3D-Heisenberg class to the 3D-Ising one as the reduced temperature approaches zero. The reduced temperature t_x at which this crossover takes place is given by $|t_x| = |H_A/H_E|^{0.8}$ [31]. For the case of $KNiF_3$ $|t_x| = 2 \times 10^{-4}$ which is precisely the limit of our fitting for $T > T_N$. This means that we are hinting this anisotropy in our experimental results, as they only slightly deviate from the Heisenberg values.

Fig. 2c and d shows the result of the fittings for thermal diffusivity. The values of the critical parameters, the fitting ranges and the quality of the fittings given by the root mean square value are also presented in Table 2. The values of the critical exponent $b = -0.099 \pm 0.004$ and the ratio of the coefficients $U^+/U^- = 1.77 \pm 0.05$ also point to the 3D Heisenberg universality class, with deviations due to the mentioned small uniaxial anisotropy (for the Ising universality class, the theoretical value is $U^+/U^- = 2.0$).

With the fitted results shown in Table 2, we see that the parameters approximately fulfill Eq. (5) as $b = -0.099 \approx \alpha = -0.110$, $U^+ = 0.554 \approx -K\ A^+/\rho B^2 = 0.663$, $U^- = 0.308 \approx -K\ A^-/\rho B^2 = 0.512$, $V = 2.173 \approx K/\rho B = 2.100$, and $W = -4.18$ but $-KC/\rho B^2 = -1.26$. U^- and W contain the biggest discrepancy, again due to the small deviation from the pure Heisenberg universality class.

Now we will turn our attention to $KCoF_3$. Fig. 3a shows the fitted curve for specific heat superimposed to the experimental data points. The curvature at $T > T_N$ cannot be adequately fitted with Eq. (1), as the fitting is done at the same time for both branches with common critical parameters. The best fit gives values for the critical exponent $\alpha = -0.081 \pm 0.01$ and for the ratio of the coefficients $A^+/A^- = 1.19 \pm 0.17$ which further deviate from the 3D-Heisenberg model and whose fitting quality is worse than in the case of $KNiF_3$. This is clearly seen not only in the deviation plots (Fig. 3b) but also in the root mean square value in Table 3 if we compare it with the one obtained for $KNiF_3$ in Table 2. Table 3 also displays all the values of the parameters for $KCoF_3$, as well as their errors, which are also worse than for $KNiF_3$. In any case, the fitting is good enough to extract the critical parameters for this material from Eq. (1).

In $KCoF_3$ the spins are ordered along the z-axis; as the single crystal sample turns multidomain at the critical temperature, the average should give a Heisenberg behaviour. Besides, even in monodomain samples, measurements on linear birefringence obtained the same critical parameter for both $KNiF_3$ and $KCoF_3$ [13].

But there is an important difference between $KNiF_3$ and $KCoF_3$, as the transition in the latter is not purely magnetic: there is also a distortion of the crystal lattice from cubic to tetragonal [19,21], whose origin lies in the spin orbit interaction. The Co^{2+} ion possess in the cubic field a threefold orbitally degenerate ground state. For these ions, degeneracy can be removed by two means: the Jahn–Teller effect and the spin–orbit interaction. An ion of Co^{2+} can be analyzed as a single hole in the t_{2g} level. During tetragonal deformation with $c/a > 1$, the Jahn–Teller effect stabilizes the hole-orbital $Id_{xy}>=Il^z - 0>$. Since the ground state has a zero orbital moment, the spin–orbit interaction is ineffective. For a tetragonal deformation where $c/a < 1$ (which is the case of $KCoF_3$ [21,32]), the doublet $Il^z = 1>$ appears to be lower. However, for this case we have a ground state characterized by an unquenched orbital momentum, and the spin–orbit interaction leads to the splitting of this level. In $KNiF_3$ the spin–orbit interaction is negligible, that's why this mechanism is not important in that case.

Usually, the transition leading to the disappearance of degeneracy by the spin–orbit effect takes place simultaneously with the magnetic ordering. This conclusion follows from the analysis of the Hamiltonian, which depends on both the spin and the orbital variables. These variables, due to the exchange interaction and the spin–orbit interaction, are markedly interrelated. Consequently, we deal not only with magnetic ordering, but also with orbital ordering which, in its turn, produces the distortion of the crystal lattice.

For the calculation of the magnetic susceptibility of these magnetic systems Suzuki et al. [33] applied the correlated effective field approximation method (CEFA) with the following Hamiltonian:

$$H = \sum_i H_i + J \sum_{<ij>} \boldsymbol{s_i} \cdot \boldsymbol{s_j} \tag{6}$$

$$H_i = \Lambda \boldsymbol{l_i} \cdot \boldsymbol{s_i} + c l_{iz}^2 \tag{7}$$

Table 2
Critical parameters and quality of the fittings (given by the root mean square value) for $KNiF_3$.

	α	A^+/A^-	T_N (K)	B (J kg^{-1} K^{-1})	C (J kg^{-1} K^{-1})	A^- (J kg^{-1} K^{-1})	E^-	E^+	RMS
c_p (J kg^{-1} K^{-1})	−0.110 ± 0.003	1.30 ± 0.03	245.22	1029 ± 4	619 ± 8	−250 ± 4	−0.400 ± 0.006	−0.240 ± 0.026	0.9983
	b	U^+/U^-	T_N (K)	V (mm^2/s)	W (mm^2/s)	U^- (mm^2/s)	F^-	F^+	RMS
D (mm^2/s)	−0.099 ± 0.004	1.77 ± 0.05	245.04	2.173 ± 0.009	−4.18 ± 0.03	0.308 ± 0.007	2.5 ± 0.1	1.31 ± 0.04	0.9996

Table 3
Critical parameters and quality of the fittings (given by the root mean square value) for $KCoF_3$.

	α	A^+/A^-	T_N (K)	B (J kg^{-1} K^{-1})	C (J kg^{-1} K^{-1})	A^- (J kg^{-1} K^{-1})	E^-	E^+	RMS
c_p (J kg^{-1} K^{-1})	−0.081 ± 0.010	1.19 ± 0.17	115.53	1016 ± 40	603 ± 10	−456 ± 37	−0.63 ± 0.06	0.05 ± 0.02	0.99466
	b	U^+/U^-	T_N (K)	V (mm^2/s)	W (mm^2/s)	U^- (mm^2/s)	F^-	F^+	RMS
D (mm^2/s)	−0.082 ± 0.011	1.26 ± 0.20	115.35	0.7 ± 0.2	−1.9 ± 0.1	2.2 ± 0.2	−0.08 ± 0.01	−0.13 ± 0.06	0.99166

where J is the exchange constant between nearest–neighbour spins (next-nearest neighbour interactions are completely negligible in these materials), $\boldsymbol{s_i}$, $\boldsymbol{s_j}$ stand for the spins vectors, $\boldsymbol{l_i}$ for the orbital angular momentum vector, Λ is the coefficient of the spin–orbit coupling for the T_1 state, l_{iz} is the z-component of the orbital angular momentum vector, being z the tetragonal axis. The second term of Eq. (7) represents the effect of a tetragonal crystalline field, where c is a parameter determined within the CEFA model. It may therefore be concluded that the lattice distortion occurs at the Néel point, and that it is the result of the magnetic properties of the system studied. The consequence is that the critical behaviour cannot be adequately described by the Heisenberg model, where the hamiltonian only includes the second term in Eq. (6); our experimental results corroborate this point.

As a checking point, we have studied the possibility of the presence of a crossover temperature from the 3D-Heisenberg model to the 3D-Ising, as renormalization group theory suggests. As there is no information available about the values of the anisotropy field H_A and the exchange field H_E in $KCoF_3$ we cannot evaluate the crossover temperature t_x but we have performed fittings using different regions without finding any crossover.

Fig. 3c and d shows the thermal diffusivity, the fitting using Eq. (2) and the corresponding deviation plot for $KCoF_3$ (all fitting parameters are presented in Table 3). The critical exponent and the ratio of the coefficients again deviate from the Heisenberg model and, what's also important, Eq. (5), which approximately hold for the Heisenberg case, are not fulfilled, there are strong deviations.

Lastly, the different behaviour shown by both materials in thermal conductivity below the phase transition (the change in slope in the case of $KNiF_3$ is much bigger than in $KCoF_3$) can also be explained due to the unquenched orbital angular momentum in the latter case. Heat carriers in these insulator materials are mainly phonons, which means that the different scattering mechanisms that can take place in them will affect the value of thermal conductivity and its evolution with temperature. If phonon–phonon interaction is the main scattering mechanism, as temperature is reduced there will be a quick increase in thermal conductivity, more rapidly than $1/T$, exponential at low enough temperatures [34]. But if there are other limiting mechanisms which reduce the phonon mean free path, such as phonon-magnon interactions, the increase in thermal conductivity as temperature is lowered will be severely reduced. In the case of $KCoF_3$ it has been experimentally [35] and theoretically [36] proved the presence of a strong phonon-magnon interaction due to its orbital angular momentum, as opposed to other similar systems without it ($RbMnF_3$, $KMnF_3$ which are similar in this aspect to $KNiF_3$ as its spin–orbit coupling is negligible). This strong interaction may have two origins: the fluctuations in the crystal field or the modulation of the exchange interactions, in both cases due to the motion of the atoms. Buyers et al. showed that the crystal field effect was important while the second effect was not, due to a lack of evidence for anisotropic exchange in spin wave measurements [36]. Thus, phonon–phonon scattering is the dominating effect to limit the phonon-mean free path in $KNiF_3$ while a strong phonon-magnon scattering takes place in $KCoF_3$, reducing the phonon mean free path. This is the reason why, from the paramagnetic phase to the antiferromagnetic one, the thermal conductivity in $KCoF_3$ increases slowlier than in the case of $KNiF_3$.

5. Conclusions

Critical behaviour of the antiferromagnetic transition in $KNiF_3$ and $KCoF_3$ has been studied by means of a high resolution photopyroelectric technique, measuring specific heat, thermal diffusivity and thermal conductivity in the close vicinity of the Néel temperatures. In the case of $KNiF_3$, it has been shown that its critical behaviour slightly deviates from the perfect Heisenberg universality class, due to its small uniaxial anisotropy (in contrast to perfect Heisenberg systems such as $RbMnF_3$ and $KMnF_3$); this behaviour has been confirmed by the interrelation among the critical parameters of the different thermal variables. In the case of $KCoF_3$, its critical behaviour has a stronger deviation from the Heisenberg universality class due to the spin–orbit interaction, which introduces a perturbation in the Hamiltonian which cannot be described by a pure Heisenberg model. This work corrects previous assumptions and results in literature, where both $KCoF_3$ and $KNiF_3$ have been considered so far as perfect 3D-Heisenberg antiferromagnets. In order to reveal their real critical behaviour, high resolution techniques must be employed.

Acknowledgments

This work have been supported by the Ministerio de Ciencia e Innovación (MAT2011-23811), Gobierno Vasco (IT619-13), and UPV/EHU (UFI11/55).

References

[1] G. Hayatulla, R. Murtaza, S. Khenata, A.H. Muhammad, K.M. Resnak, S. Wong, Bin Omran, Z.A. Alahmed, Comput. Mater. Sci. 85 (2014) 402.
[2] J.M. Yeomans, Statistical Mechanics of Phase Transitions, Oxford University Press, 2002.
[3] M. Marinelli, F. Mercuri, S. Foglietta, D.P. Belanger, Phys. Rev. B 54 (1996) 4087.
[4] A. Salazar, M. Massot, A. Oleaga, A. Pawlak, W. Schranz, Phys. Rev. B 75 (2007) 224428.
[5] A. Oleaga, A. Salazar, Yu.M. Bunkov, J. Phys.: Condens. Matter 26 (2014) 096001.
[6] M. Marinelli, F. Mercuri, D.P. Belanger, Phys. Rev. B 51 (1995) 8897.
[7] A. Oleaga, A. Salazar, D. Prabhakaran, J.G. Cheng, J.S. Zhou, Phys. Rev. B 85 (2012) 184425.
[8] A. Kornbli, G. Ahlers, Phys. Rev. B 8 (1973) 5163.
[9] A. Tucciarone, H.Y. Lau, L.M. Corliss, A. Delapalme, J.M. Hastings, Phys. Rev. B 4 (1971) 3206.
[10] H. Yamaguchi, K. Katsumata, M. Hagiwara, M. Tokunaga, Phys. Rev. B 59 (1999) 6021.
[11] D.G. Money, D.M. Paige, W.D. Corner, B.K. Tanner, J. Magn. Magn. Mater. 15–18 (1980) 603.
[12] C.C. Becerra, Y. Shapira, N.F. Oliveira Jr, Phys. Rev. B 18 (1978) 5060.
[13] J. Ferre, J.P. Jamet, Solid State Commun. 44 (1982) 485.
[14] K. Saiki, H. Yoshiosa, Sol. State Commun. 15 (1974) 1067.
[15] K. Hirakawa, T. Hashimoto, K. Hirakawa, J. Phys. Soc. Jpn. 16 (1961) 1935.
[16] M.J. Freiser, P.E. Seiden, D.T. Teaney, Phys. Rev. Lett. 10 (1963) 293.
[17] K. Saiki, K. Horai, H. Yoshioka, J. Phys. Soc. Jpn. 35 (1973) 1016.
[18] D. Skrzypek, P. Jakubowski, A. Ratuszna, A. Chełkowski, J. Cryst. Growth 48 (1980) 475.
[19] A. Ratuszna, A. Pietraszko, A. Chełkowski, K. Łukaszewicz, Phys. Stat. Sol. (a) 54 (1979) 739.
[20] A. Ratuszna, D. Skrzypek, J. Kapusta, Phase Transitions 42 (1993) 189.
[21] A. Okazaki, Y. Suemune, J. Phys. Soc. Jpn. 16 (1961) 671.

[22] M. Marinelli, U. Zammit, F. Mercuri, R. Pizzoferrato, J. Appl. Phys. 72 (1992) 1096.
[23] M. Chirtoc, D. Dadarlat, D. Bicanic, J.S. Antoniow, M. Egée, in: A. Mandelis, P. Hess (Eds.), Progress in Photothermal and Photoacoustic Science and Technology, vol. 3, SPIE, Bellingham, Washington, 1997.
[24] S. Delenclos, M. Chirtoc, A. Hadj Sahraoui, C. Kolinsky, J.M. Buisine, Rev. Sci. Instrum. 73 (2002) 2773.
[25] A. Salazar, Rev. Sci. Instrum. 74 (2003) 825.
[26] M. Marinelli, F. Mercuri, U. Zammit, R. Pizzoferrato, F. Scudieri, D. Dadarlat, Phys. Rev. B 49 (1994) 9523.
[27] A. Kornblit, G. Ahlers, Phys. Rev. B 11 (1975) 2678.
[28] K. Hirakawa, K. Irakawa, T. Hashimoto, J. Phys. Soc. Jpn. 15 (1960) 2063.
[29] J. Nouet, A. Zarembowitch, R.V. Pisarev, J. Ferre, M. Lecomte, Appl. Phys. Lett. 21 (1972) 161.
[30] F. Ganot, C. Dugautier, P. Moch, J. Nouet, J. Phys. C: Solid State Phys. 15 (1982) 801.
[31] M.E. Fisher, Rev. Mod. Phys. 46 (1974) 597.
[32] J. Julliard, J. Nouet, Rev. Phys. Appliquée 10 (1975) 325.
[33] N. Suzuki, T. Isu, K. Motizuki, Sol. State Commun. 23 (1977) 319.
[34] R. Berman, Thermal Conduction in Solids, Oxford University Press, 1979.
[35] T.M. Holden, W.J.L. Buyers, E.C. Svensson, R.A. Cowley, M.T. Hutchings, D. Hukin, R.W.H. Stevenson, J. Phys. C: Solid State Phys. 4 (1971) 2127.
[36] W.J.L. Buyers, T.M. Holden, E.C. Svensson, R.A. Cowley, M.T. Hutchings, J. Phys. C: Solid State Phys. 4 (1971) 2139.